# Uniaxial indefinite material formed by helical-shaped wires

## Tiago A Morgado, Stanislav I Maslovski and Mário G Silveirinha

Department of Electrical Engineering, Instituto de Telecomunicações,
University of Coimbra, 3030 Coimbra, Portugal
E-mail: tiago.morgado@co.it.pt, stas@co.it.pt and mario.silveirinha@co.it.pt

**Abstract.** We demonstrate that a racemic array of helical-shaped metallic wires may be regarded as a local uniaxial epsilon-negative (ENG) material even when the metal conductivity is very large (e.g. in the microwave regime) and, as a result, enables strong negative refraction over a wide frequency range. Based on the negative refraction effect, we demonstrate partial focusing of *p*-polarized electromagnetic radiation using a planar lens formed by such a composite material. The results reported here are supported by full-wave simulations as well as by analytical calculations based on effective medium theory.

**Contents**

## 1. Introduction

The phenomenon of negative refraction continues to attract much interest in the scientific community owing to its intriguing and counterintuitive properties. This unusual effect may be observed, for example, when light is refracted at interfaces between conventional dielectrics and materials with simultaneously negative permittivity and permeability (negative index of refraction), and was described by Veselago in 1968 [1]. However, since there are no naturally available materials with a negative isotropic index of refraction, Veselago's work was consigned to oblivion until the end of the last century, when a study published by Pendry [2]—which resulted in the subsequent development of artificially designed materials (metamaterials) [3]—brought it into the limelight. Since then, the negative refraction of electromagnetic waves using artificially structured materials with negative index of refraction has been experimentally verified for microwaves [4] and more recently in the optical domain [5]. Nevertheless, this class of artificial media is strongly sensitive to losses and material dispersion [6, 7], and hence, alternative possibilities to achieve negative refraction have been studied, namely using photonic crystals [8, 9], non-local materials [10, 11], chiral media [12–14] and even nonlinear phase-conjugating metamaterials [15–17].

Yet another robust solution for achieving negative refraction is through the use of anisotropic indefinite media, such that the principal components of the permittivity and/or permeability tensors have different signs [18–25]. In particular, the negative refraction effect based on an indefinite anisotropic material was recently demonstrated in the optical domain using an array of metallic nanorods [24, 25]. Due to the large kinetic inductance associated with the electron plasma in metals in the optical regime, this structure may indeed behave as an indefinite medium, such that the effective permittivity along the direction parallel to the wires is negative, whereas the permittivity is positive along directions perpendicular to the wires. Hence, such a configuration may provide broadband all-angle negative refraction and partial focusing of *p*-polarized waves [24, 25]. However, at lower frequencies (microwave and low infrared frequencies), the effect of kinetic inductance disappears owing to the large conductivity of the metals, so that the array of nanowires acquires a strongly spatially dispersive response [26] and behaves very differently from in the optical domain. Thus, negative refraction is hindered in the indicated spectral range.

Despite these difficulties, it has been proposed [27] that at microwave and terahertz frequencies the spatial dispersion effects can be tamed simply by increasing either the capacitance or the inductance of the wires, without resorting directly to the transport properties of electrons in metals. The capacitance may be increased by attaching metallic plates to the wires, whereas the inductance may be increased either by coating the wires with a magnetic material or by loading the wires with bulk inductors. The first possibility was further developed in several works [28–32], and a strong negative refraction effect in a wire medium with attached metallic patches was numerically demonstrated in [33, 34]. Even though very effective, this approach has a drawback: attaching plates to the wires may dramatically increase the transverse permittivity of the medium, which is undesirable because it deteriorates the impedance matching with the external medium and, consequently, reduces the available bandwidth. On the other hand, the second approach based on wires coated with a magnetic material is impractical, due to the difficulty in finding materials with the desired magnetic response.

Here, we suggest an alternative way to increase the inductance of the wires, and thereby suppress the spatial dispersion effects, which is based on shaping the geometry of the wires: we
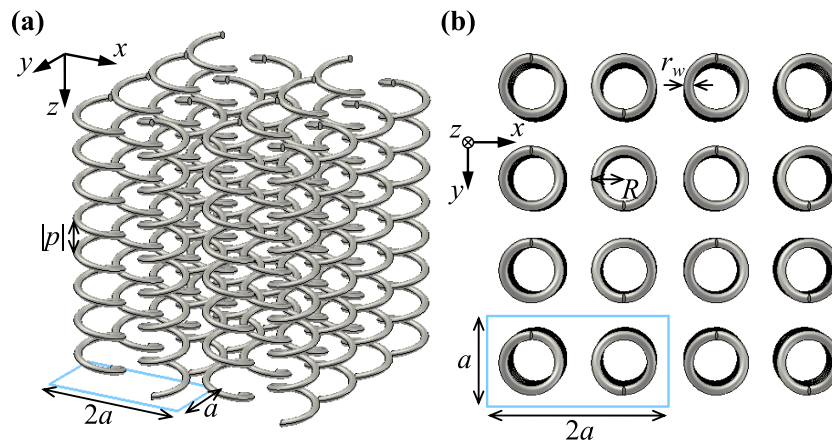
**Figure 1.** Geometry of the non-bianisotropic (racemic) helical wire medium: a periodic array of metallic helices arranged in a rectangular lattice (2*a* along the *x*-direction and *a* along the *y*-direction). Each unit cell includes two helices with opposite handedness, i.e. a right-handed helix and a left-handed helix. (a) Perspective view. (b) Top view. *R* represents the radius of the helices and $r_w$ is the wire radius. Without loss of generality, it is assumed that the helices stand in free-space.

consider a metamaterial formed by a racemic mixture of left- and right-handed long metallic helices. Such a solution may provide a smaller value for the transverse effective permittivity compared with the approach based on attaching plates to the wires and consequently a broader bandwidth of operation. In this work, we investigate in detail the macroscopic response of an array of long metallic helices, and study the possibility of negative refraction and partial focusing. It is shown that under certain conditions, the material may behave as an indefinite uniaxial medium with a local response at microwave and low infrared frequencies.

This paper is organized as follows. In section 2, the geometry of the metamaterial is described and a homogenization model that characterizes its electromagnetic response is introduced. Then, in section 3 the scattering of electromagnetic waves by the metamaterial is characterized using the developed homogenization model. In particular, the possibility of suppressing the spatial dispersion effects is discussed. In section 4, the emergence of negative refraction at the interface of the metamaterial with air is investigated. In section 5, we study the focusing of the fields radiated by a magnetic line source by a flat slab of the metamaterial. Finally, in section 6 conclusions are drawn.

In this work, we assume that the fields are monochromatic and that the time dependence is $e^{j\omega t}$.

## 2. Homogenization model of a racemic helical wire medium

We consider an array of long metallic helices with the axis along the *z*-direction (figure 1). Related structures have been considered previously in the context of bianisotropic arrays [35], broadband circular polarizers [36–38] and wave plates [39]. In contrast, here we study the possibility of using helical wires to suppress the spatial dispersion effects that are inherent to wire media at low frequencies (microwave and low infrared frequencies). Moreover, the helical

wire medium considered here is different from that considered in [37–39]. Indeed, whereas in [37–39] the helices have fixed handedness, here the helices are of two types: right-handed and left-handed helices are alternately packed in a lattice, in such a manner that the unit cell is rectangular (dimension $2a$ along the $x$-direction and $a$ along the $y$-direction) and includes two helices with opposite handedness within the same cell (figure 1). In other words, this structure is a racemic mixture of left- and right-handed inclusions. The radius of the helices is $R$ and the wire's radius is $r_w$. The metamaterial is obtained by a periodic repetition of the unit cell defined by the primitive vectors $\mathbf{a}_1 = 2a\,\hat{\mathbf{u}}_x$, $\mathbf{a}_2 = a\hat{\mathbf{u}}_y$ and $\mathbf{a}_3 = |p|\,\hat{\mathbf{u}}_z$, where $p$ represents the helix pitch. Since the unit cell has inversion symmetry, the response of the metamaterial is non-bianisotropic.

In what follows, we obtain an effective medium model for the metamaterial of figure 1. Our derivation is based on the results of [40], wherein the effective response of the artificial medium formed by an array of perfectly electrical conducting (PEC) helical-shaped wires (helices) with *a fixed handedness* was characterized. The model of [40] is based on a non-local (spatially dispersive) dielectric function $\bar{\bar{\varepsilon}}(\omega, \mathbf{k})$, where $\omega$ is the frequency and $\mathbf{k}$ is the wave vector, that fully characterizes the macroscopic response of the metamaterial [41]. In the same work [40], analytical expressions for the conventional material parameters (effective permittivity, effective permeability and magnetoelectric coupling parameters) are also derived. These parameters are linked to the dielectric function $\bar{\bar{\varepsilon}}(\omega, \mathbf{k})$ as follows [40, 41]:

$$\frac{\bar{\bar{\varepsilon}}}{\varepsilon_0}(\omega, \mathbf{k}) = \bar{\bar{\varepsilon_r}} - \bar{\bar{\xi}} \cdot \bar{\bar{\mu_r}}^{-1} \cdot \bar{\bar{\zeta}} + \left( \bar{\bar{\xi}} \cdot \bar{\bar{\mu_r}}^{-1} \times \frac{\mathbf{k}}{k_0} - \frac{\mathbf{k}}{k_0} \times \bar{\bar{\mu_r}}^{-1} \cdot \bar{\bar{\zeta}} \right) + \frac{\mathbf{k}}{k_0} \times \left( \bar{\bar{\mu_r}}^{-1} - \bar{\bar{\mathbf{I}}} \right) \times \frac{\mathbf{k}}{k_0}, \qquad (1)$$

where $\bar{\bar{\varepsilon_r}}$ is the relative permittivity tensor, $\bar{\bar{\mu_r}}$ is the relative permeability tensor, $\bar{\bar{\xi}}$ and $\bar{\bar{\zeta}}$ are dimensionless parameters that characterize the magnetoelectric coupling, $k_0 = \omega\sqrt{\varepsilon_0\mu_0}$ is the free-space wave number, and $\bar{\bar{\mathbf{I}}}$ is the identity dyadic. Explicit formulae for these material parameters can be found in [40] (the formulae for the permittivity and permeability are also provided below).

We want to make a connection between the effective medium parameters derived in [40] and those associated with the geometry of figure 1 where the helices have no fixed handedness. Our theory is based on the hypothesis that the parameters $\bar{\bar{\varepsilon_r}}$ and $\bar{\bar{\mu_r}}$ have the same expression, independent of the handedness of the helices in the array being fixed (as in [40]) or not fixed (as in this work). Hence, from the theory of [40], equation (20), it is possible to write that

$$\bar{\bar{\varepsilon_r}} = \varepsilon_t \left( \hat{\mathbf{u}}_x \hat{\mathbf{u}}_x + \hat{\mathbf{u}}_y \hat{\mathbf{u}}_y \right) + \varepsilon_{zz} \hat{\mathbf{u}}_z \hat{\mathbf{u}}_z,$$

$$\varepsilon_{zz} = 1 - \frac{1}{\frac{k_0^2}{\beta_{p1}^2} - \frac{k_z^2}{\beta_{p2}^2}} + \frac{A^2 k_0^2}{\left( 1 + \frac{A^2 k_0^2}{\frac{k_0^2}{\beta_{p1}^2} - \frac{k_z^2}{\beta_{p2}^2}} \right) \left( \frac{k_0^2}{\beta_{p1}^2} - \frac{k_z^2}{\beta_{p2}^2} \right)^2}, \qquad (2)$$

$$\bar{\bar{\mu_r}} = \hat{\mathbf{u}}_x \hat{\mathbf{u}}_x + \hat{\mathbf{u}}_y \hat{\mathbf{u}}_y + \mu_{zz} \hat{\mathbf{u}}_z \hat{\mathbf{u}}_z,$$

$$\mu_{zz} = \frac{1}{1 + \frac{A^2 k_0^2}{\frac{k_0^2}{\beta_{p1}^2} - \frac{k_z^2}{\beta_{p2}^2}}}. \qquad (3)$$

**IOP** Institute of Physics $\Phi$ DEUTSCHE PHYSIKALISCHE GESELLSCHAFT

where $A = \pi R^2/p$ and

$$\varepsilon_t = 1 + \frac{(\pi R)^2}{V_{\text{cell}}} \frac{1}{C_1}, \tag{4}$$

$$\beta_{p1} = \sqrt{\frac{(2\pi p)^2}{C_0 p^2 V_{\text{cell}} + 8C_1 \pi^2 R^2 V_{\text{cell}}}}, \tag{5}$$

$$\beta_{p2} = \sqrt{\frac{(2\pi)^2}{C_0 V_{\text{cell}}}}. \tag{6}$$

$V_{\text{cell}} = a^2|p|$ is the volume of the unit cell, and $C_0$ and $C_1$ are parameters that only depend on the geometry of the artificial material and whose definitions may be found in [40]. The parameters $C_0$ and $C_1$ need to be evaluated numerically [40].

On the other hand, because in reciprocal media the magnetoelectric coupling (gyrotropy) can only be observed in structures without a center of symmetry [42], it should be clear that $\overline{\overline{\xi}} = -\overline{\overline{\zeta}}^T = 0$ in the case that the helices have no fixed handedness, as assumed here.

As one can see, similar to the configuration with helices with a fixed handedness [40], the permittivity and permeability tensors of the metamaterial with suppressed bianisotropic effects are spatially dispersive. Indeed, equations (2) and (3) depend explicitly on $k_z$ ($z$-component of the wave vector). Nevertheless, in the case that $\beta_{p2}$ is much greater than $k_z$ ($\beta_{p2} \gg k_z$), the term $k_z^2/\beta_{p2}^2$ may be discarded and hence $\overline{\overline{\varepsilon_r}}$ and $\overline{\overline{\mu_r}}$ become exclusively frequency dependent, which means that the electromagnetic response of the metamaterial is local. In particular, the dielectric tensor is anisotropic and indefinite. This issue will be further discussed later in this paper.

## 3. Requirements for a quasi-local response

The goal of this section is to study the dispersion characteristics of the plane waves supported by the racemic helical wire medium (figure 1). Since equations (2) and (3) establish that the effective medium behaves as a uniaxial non-bianisotropic magneto-dielectric material with the optical axis along the $z$-direction, it follows that the plane waves can be classified as either transverse magnetic to $z$ (TM-$z$)-polarized waves (or $p$-polarized waves) or transverse electric to $z$ (TE-$z$)-polarized incident waves (or $s$-polarized waves). As is well known, the dispersion of the TM and TE waves in such a material is given by [43]

$$k_0^2 \varepsilon_t - \frac{\varepsilon_t}{\varepsilon_{zz}} k_t^2 - k_z^2 = 0 \quad \text{(TM waves)} \tag{7}$$

$$k_0^2 \varepsilon_t - \frac{1}{\mu_{zz}} k_t^2 - k_z^2 = 0 \quad \text{(TE waves)} \tag{8}$$

where $k_t^2 = k_x^2 + k_y^2$, $\varepsilon_t$ is defined by equation (4) and $\varepsilon_{zz}$ and $\mu_{zz}$ are given by equations (2) and (3). It can be shown that due to the spatial dispersion effects both the characteristic equations (7) and (8) reduce to a second-order degree polynomial in the variables $k_0^2$ and $k_z^2$. Thus, the homogenization model predicts that the structured medium supports four independent plane waves, i.e. for a fixed frequency it supports four independent eigenmodes: two associated with TM-polarized waves and two associated with TE-polarized waves.
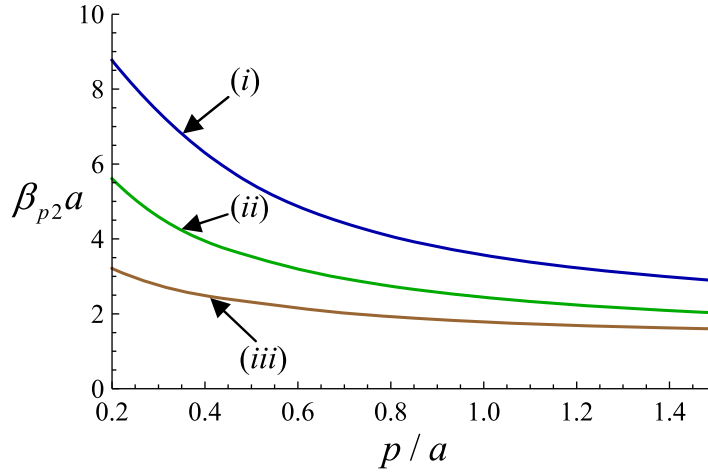
**Figure 2.** $\beta_{p2}$ as a function of the normalized helix pitch $p$ for different geometries, calculated using equation (6). (i) $R = 0.4a$ and $r_w = 0.05a$; (ii) $R = 0.4a$ and $r_w = 0.01a$; (iii) $R = 0.2a$ and $r_w = 0.01a$.

In this paper, we are only interested in the case of propagation in the *xoz*-plane ($k_y = 0$) with the magnetic field along the *y*-direction (TM-*z* polarized wave). In such circumstances, the dispersion characteristic of the plane waves supported by the effective medium reduces to a polynomial equation of second degree in the variable $k_0^2$

$$-\left(A^2\beta_{p1}^2\beta_{p2}^2\varepsilon_t + \beta_{p2}^2\varepsilon_t\right)k_0^4 + \left(A^2 k_x^2\beta_{p1}^2\beta_{p2}^2\varepsilon_t + A^2 k_z^2\beta_{p1}^2\beta_{p2}^2 + k_x^2\beta_{p2}^2\varepsilon_t \right.$$
$$\left. + k_z^2\beta_{p1}^2\varepsilon_t + k_z^2\beta_{p2}^2 + \beta_{p1}^2\beta_{p2}^2\varepsilon_t\right)k_0^2 - k_z^2\beta_{p1}^2\beta_{p2}^2 - k_x^2 k_z^2\beta_{p1}^2\varepsilon_t - k_z^4\beta_{p1}^2 = 0. \tag{9}$$

Hence, in agreement with equation (7), the above equation predicts that the metamaterial supports two distinct plane wave modes with magnetic field along the *y*-direction. The emergence of an additional eigenwave is a consequence of the spatially dispersive response. Note that in conventional local materials each fixed polarization is associated with a single plane wave mode. Nevertheless, it is expected that for large values of $\beta_{p2}$ the contribution of the high-frequency mode may be discarded, and the medium may have a quasi-local response.

How can one get large values for $\beta_{p2}$ in practice? Equation (6) shows that the parameter $\beta_{p2}$ is inversely proportional to $C_0$ and $V_{cell}$. Thus, in order that $\beta_{p2}$ is large we are interested in geometries for which $C_0$ and $V_{cell}$ are as small as possible. For a fixed lattice constant $a$, one can get small values for $V_{cell}$ by considering helices with short pitch $p$. On the other hand, as one can see from figure 2 of [40], a small value for the constant $C_0$ requires larger values of the radius $R$ of the helices. Thus, the relevant geometries are such that the helices have a short pitch and a large radius.

In these conditions, the spatial dispersion term $k_z^2/\beta_{p2}^2$ in the analytical expression of $\varepsilon_{zz}$ may be discarded and the macroscopic response of the structured material becomes solely frequency dependent and is characterized by the following expression:

$$\varepsilon_{zz}^{loc} = 1 - \frac{\beta_{p,eff}^2}{k_0^2}, \tag{10}$$

where $\beta_{p,\text{eff}}$ is the plasma wave number of the effective medium and is given by

$$\beta_{p,\text{eff}} = \beta_{p1}/\sqrt{1 + A^2 \beta_{p1}^2}. \tag{11}$$

It is interesting to establish a parallelism with the quasistatic homogenization model for general wire media introduced in [28], where the spatial dispersion effects were shown to be dependent on a slow-wave factor $n = \sqrt{LC/(\varepsilon_0\mu_0)}$, where $L$ and $C$ represent the effective inductance and capacitance per unit length of the wires, respectively. As discussed in [28], the spatial dispersion effects become negligible when the slow-wave factor is much larger than unity. A straightforward analysis shows that in our material formed by helical shaped wires, the slow-wave factor is equal to $\beta_{p2}/\beta_{p1}$. In the racemic helical wire medium large values of the slow-wave factor are achieved mainly due to an increase of the effective inductance of the wires, as a result of the current flowing along the helices that creates a magnetic field and, consequently, a magnetic flux. However, the effective capacitance per unit length of the helical wires may also increase, simply because the wire surface area where the electric charge accumulates is larger per unit length of a helix than per unit length of a straight wire, and hence it may also contribute to the suppression of the spatial dispersion effects.

In the standard wire medium formed by straight metallic wires the spatial dispersion effects emerge because the wires span the entire unit cell, and as a consequence the response of the wires is strongly sensitive to gradients $(d/dz)$ of the electric field across the unit cell [44]. This is so because each inclusion can strongly interact with the $z$-component of the microscopic electric field in the entire unit cell. On the other hand, if we consider helical-shaped wires instead of straight wires, the interaction with the $z$-component of the electric field is somewhat weakened because the wires are no longer directed along the $z$-direction. This is especially true when $|p|/(2\pi R) \ll 1$ for which the vector tangent to the helices is almost parallel to the $xoy$-plane, and hence the wires' response is not so sensitive to gradients of the electric field along $z$. This may explain in simple physical terms the reduction of the spatial dispersion in the helical wire medium.

To demonstrate the reduction of the spatial dispersion effects, we have calculated the dispersion diagrams for propagation along the $z$-direction. In figures 3(a) and (b), we depict the dispersion characteristics of the racemic helical wire medium (figure 1) with helices with radius $R = 0.4a$ and wire radius $r_{\text{w}} = 0.05a$ for two configurations with distinct values of helix pitch $p$: (a) $|p| = 0.3a$ and (b) $|p| = 0.9a$. In addition, in order that we have a benchmark for these results, we have also computed the dispersion characteristic of the standard wire medium formed by the straight wires (figure 3(c)). The dispersion curves predicted by the non-local homogenization model (equation (2)) (solid lines) and by the local homogenization model (equation (10)) (dashed lines) are compared with the full-wave results calculated using the numerical method reported in [45] (star symbols). It is seen in figure 3 that the results obtained with the three different methods predict two dispersion branches: a transverse mode or quasi-TEM mode (blue curves) and a longitudinal mode (green curves).

In figures 3(a) and (b), the agreement between the non-local homogenization model and the numerical method is particularly good for relatively low frequencies (roughly, $k_0 a < 0.8$). For higher frequencies, there is a slight lack of agreement, which is a consequence of the approximations made in the derivation of the analytical model [40]. On the other hand, there is excellent agreement between the non-local homogenization results and the full-wave results for the standard wire medium formed by straight wires, even for high frequencies
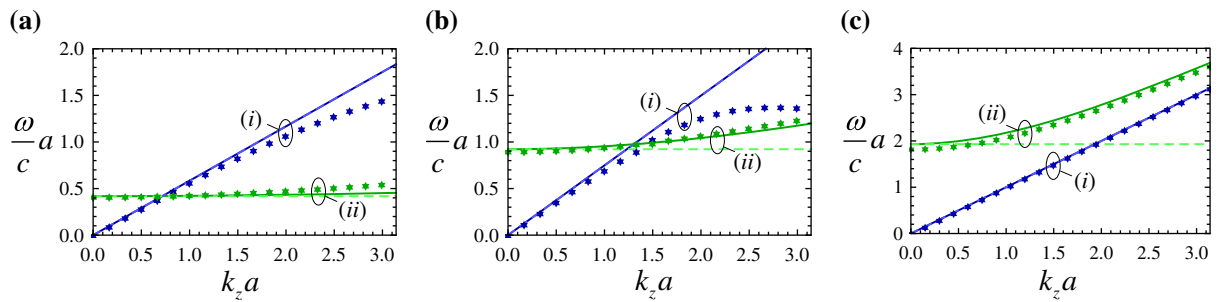
**Figure 3.** Dispersion diagrams for three different geometries of wire arrays (helical-shaped wires and straight wires). (a) Racemic helical medium with $R = 0.4a$, $r_w = 0.05a$ and $|p| = 0.3a$. (b) The same as in (b) but for $|p| = 0.9a$. (c) Standard wire medium with $r_w = 0.05a$. Solid lines: non-local homogenization results (equation (2)); dashed lines: local homogenization results (equation (10)); star symbols: full-wave numerical results. (i) Transverse mode or quasi-TEM mode and (ii) longitudinal mode. It should be noted that in the case of panel (c) (straight metallic wires), the low-frequency mode is exactly TEM.

(figure 3(c)). Regarding the local homogenization model results, they concur well with non-local model results and the full-wave simulations only for the case of helical-shaped wires with short helix pitch $p$ (figure 3(a)). In contrast, for helices with a longer helix pitch $p$ (figure 3(b)), and even more pronounced for the case of straight wires ($|p| = \infty$) (figure 3(c)), the dispersionless (flat) band predicted by the local homogenization model fails to accurately describe the behavior of the longitudinal mode. These results confirm that by decreasing the helix pitch $p$, it is indeed possible to nearly suppress the spatial dispersion effects and mimic the response of an ideal continuous indefinite medium. In particular, it is seen in figure 3(a) that the dispersion of the longitudinal mode becomes almost independent of $k_z$, and thus the group velocity $v_g = d\omega/dk_z$ is nearly zero. In such circumstances, the non-bianisotropic helical wire medium may be regarded as a local uniaxial epsilon-negative (ENG) material.

To further demonstrate this, the effective permittivity components $\varepsilon_{xx} = \varepsilon_{yy}$ and $\varepsilon_{zz}$ are depicted in figure 4 as a function of the frequency. The accuracy of the analytical results calculated from equations (4) and (10) is checked against results obtained with the full-wave homogenization method proposed in [41]. As seen in figure 4, there is very good agreement between the two approaches. Moreover, it is evident that for $\omega a/c < 0.4$, the structured material is a uniaxial indefinite material with $\varepsilon_{zz} < 0$ and $\varepsilon_{xx} > 0$.

## 4. Negative refraction

Next, we investigate the negative refraction effect at the interface of the proposed structured material with air. As shown in figure 4, for low frequencies the artificial medium has $\varepsilon_{zz} < 0$ and $\varepsilon_{xx} > 0$, and hence one may expect that the metamaterial may negatively refract $p$- (TM-$z$)-polarized waves [19].
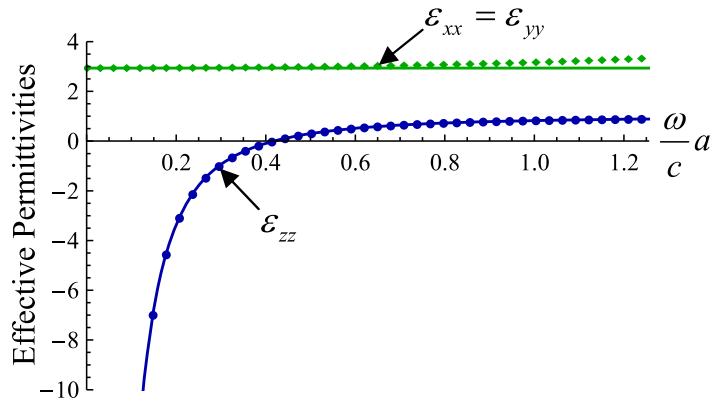
**Figure 4.** Effective permittivity components as a function of the normalized frequency for a racemic helical wire medium (figure 1) with $R = 0.4a$, $r_{\mathrm{w}} = 0.05a$ and $|p| = 0.3a$. The solid lines correspond to the analytical results and are obtained using equations (2) and (4) discarding the term $k_z^2/\beta_{p2}^2$ (or equivalently using equation (10)), whereas the discrete symbols are obtained using the full-wave homogenization approach reported in [41].
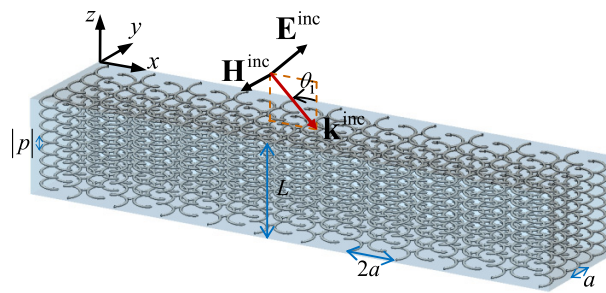


**Figure 5.** Geometry of the metamaterial slab formed by metallic helical-shaped wires. The radius of the helices is $R$ and the radius of the wires is $r_{\mathrm{w}}$. The plane of incidence is the *xoz*-plane and the wave is TM-*z*-polarized ($\mathbf{k}^{\mathrm{inc}} = (k_x, 0, k_z^{\mathrm{inc}})$, $\mathbf{H}^{\mathrm{inc}} = H^{\mathrm{inc}}\hat{\mathbf{u}}_y$).

### 4.1. The fundamental electromagnetic mode

In order to characterize the electromagnetic fields scattered by a metamaterial slab under TM-*z* excitation (figure 5), it is useful to study first the properties of the plane wave modes supported by the material.

As discussed in section 3, in general, as a consequence of spatial dispersion, for a fixed frequency the metamaterial supports two independent plane waves with magnetic field along the *y*-direction. However, the contribution of the high-frequency mode (second TM mode) may be negligible for metamaterial geometries such that the helix pitch $p$ is short. Moreover, the second TM mode is cut off for low frequencies, and typically starts propagating close to the plasma frequency $\omega/c = \beta_{p,\mathrm{eff}}$, for which $\varepsilon_{zz} = 0$. Here, we are chiefly interested in the frequency band wherein $\varepsilon_{zz} < 0$, since it is in this range of frequencies that we expect to obtain a negative refraction effect. Thus, next we concentrate our attention on the study of the properties of the fundamental mode.
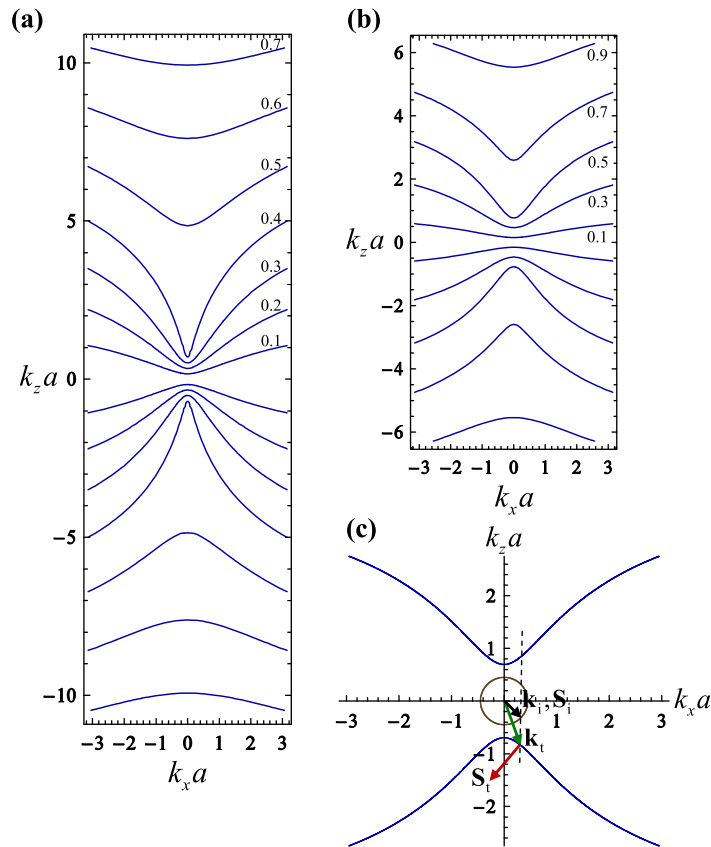
**Figure 6.** Isofrequency contours of the fundamental plane wave mode supported by the racemic helical wire medium for propagation in the *xoz*-plane with magnetic field perpendicular to this plane (figure 5). (a) $R = 0.4a$, $r_w = 0.05a$ and $|p| = 0.3a$; (b) $R = 0.4a$, $r_w = 0.05a$ and $|p| = 0.5a$. Panel (c) depicts the isofrequency contour of the fundamental mode supported by the metamaterial (blue curves) for the normalized frequency $\omega a/c = 0.45$ and for the same configuration as in (b), as well as the isofrequency contour in the air region (brown circle). The transmitted wave vector $\mathbf{k}_t$ (green arrow) is determined by the conservation of the tangential component of the wave vector $k_x$, whereas the Poynting vector $\mathbf{S}_t$ (red arrow) is normal to the isofrequency curves and is oriented toward increasing frequencies.

The isofrequency contours of the fundamental plane wave mode, calculated from equation (9), are depicted in figure 6 for two different metamaterial configurations.

As one can see from figures 6(a) and (b), the fundamental mode is characterized by hyperbolic-shaped isofrequency contours. Hence, as illustrated in figure 6(c), the Poynting vector (the energy density flux) is always negatively refracted for any angle of incidence (assuming incidence from the air side), since it must be normal to the isofrequency contours. Therefore, a TM-polarized wave is negatively refracted at the interface between air and the racemic helical wire medium.

To further characterize the negative refraction effect, we calculated the angle of refraction $\theta_t$ for the energy density flux (determined by the Poynting vector of the transmitted wave $\mathbf{S}_t$) using
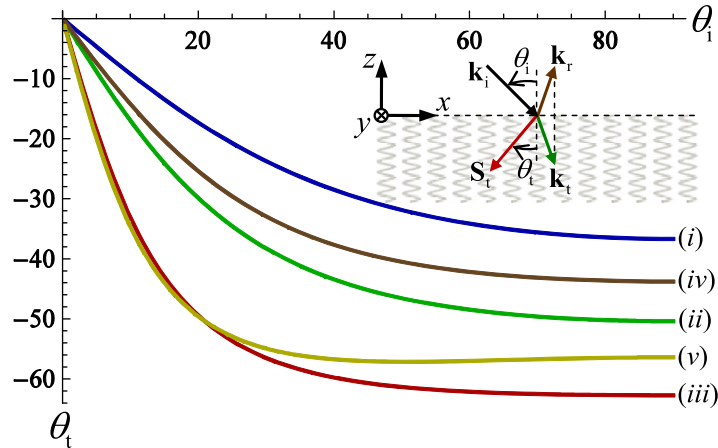
**Figure 7.** Angle of transmission of the energy density flux (the Poynting vector) as a function of the angle of incidence for different frequencies of operation and configurations. (i) $R = 0.4a$, $r_w = 0.05a$, $|p| = 0.3a$ and $\omega a/c = 0.25$; (ii) $R = 0.4a$, $r_w = 0.05a$, $|p| = 0.3a$ and $\omega a/c = 0.3$; (iii) $R = 0.4a$, $r_w = 0.05a$, $|p| = 0.3a$ and $\omega a/c = 0.35$; (iv) $R = 0.4a$, $r_w = 0.05a$, $|p| = 0.5a$ and $\omega a/c = 0.45$; (v) $R = 0.4a$, $r_w = 0.05a$, $|p| = 0.5a$ and $\omega a/c = 0.55$. The inset represents the geometry of the problem showing the incident, reflected and refracted waves.

the relation $v_g = \nabla_k \omega(\mathbf{k})$ and taking into account that the projection of the wave vector onto the interface, i.e. the $x$-component of the wave vector $k_x$, must be preserved [8]. The incoming plane wave is characterized by the wave vector $\mathbf{k}_i = \omega/c(\sin\theta_i, 0, -\cos\theta_i)$, as depicted in the inset of figure 7.

Figure 7 confirms that the angle of transmission is negative for positive angles of incidence. Therefore, consistent with the hyperbolic shaped isofrequency contours (figure 6), the Poynting vector of the transmitted wave $\mathbf{S}_t$ undergoes, indeed, negative refraction at the interface of the metamaterial with air. The negative refraction is particularly strong when the metamaterial is operated close to the plasma frequency $\omega/c = \beta_{p,\mathrm{eff}}$ (i.e. when $\varepsilon_{zz} = 0$) (curves (iii) and (v) in figure 7 for two different metamaterial configurations).

*4.2. Transmission characteristics*

Next, the transmission properties of the metamaterial slab are studied under plane wave incidence, and the negative refraction effect is characterized from the obtained transmission properties.

To begin with, we study the plane wave scattering problem using the non-local homogenization model of section 2. The metamaterial slab is assumed as infinite and periodic along the $x$- and $y$-directions with lattice periods $2a$ and $a$, respectively, and finite with thickness $L$ along the $z$-direction (figure 5). The direction of propagation of the incident wave is in the $xoz$-plane ($k_y = 0$) and the magnetic field is polarized along the $y$-direction. Thus, the magnetic field in the three regions of space can be written as follows (the $x$-dependence of the fields is

omitted):

$$H_y^{(1)} = H_y^{\text{inc}}(e^{\gamma_0 z} + \rho\, e^{-\gamma_0 z}), \quad z > 0$$

$$H_y^{(2)} = A_1^+ e^{-jk_z^{(1)}z} + A_1^- e^{+jk_z^{(1)}z} + A_2^+ e^{-jk_z^{(2)}z} + A_2^- e^{+jk_z^{(2)}z}, \quad -L < z < 0, \qquad (12)$$

$$H_y^{(3)} = H_y^{\text{inc}} t\, e^{\gamma_0(z+L)}, \quad z < -L,$$

where $H_y^{\text{inc}}$ is the incident magnetic field, $\gamma_0 = \sqrt{k_x^2 - \omega^2 \varepsilon_0 \mu_0}$ is the free-space propagation constant, $k_x = \omega\sqrt{\varepsilon_0\mu_0}\sin\theta_i$, and $\rho$ and $t$ are the reflection and transmission coefficients, respectively. The propagation constants $k_z^{(1,2)}$ (calculated by solving equation (9) with respect to $k_z$) and the amplitudes $A_{1,2}^\pm$ are associated with the two distinct modes excited inside the metamaterial slab. For each plane wave with magnetic field of the form $\mathbf{H} = H_0\, e^{-j\mathbf{k}\cdot\mathbf{r}}\hat{\mathbf{u}}_y$, the corresponding electric field is given by

$$\mathbf{E} = \frac{\eta_0 H_0}{k_0}\left(\frac{k_z}{\varepsilon_t}\hat{\mathbf{u}}_x - \frac{k_x}{\varepsilon_{zz}}\hat{\mathbf{u}}_z\right)e^{-j\mathbf{k}\cdot\mathbf{r}}. \qquad (13)$$

In order to calculate the reflection and transmission coefficients, we impose that the tangential components of the electromagnetic fields ($E_x$ and $H_y$) are continuous at the interfaces $x = 0$ and $x = -L$. As a consequence of the emergence of two plane wave modes with the same polarization, these classical boundary conditions are insufficient to determine all the unknowns of the scattering problem (equation (12)). To remove the extra degrees of freedom, the classical boundary conditions must be complemented with an additional boundary condition (ABC) at both interfaces. In particular, it is necessary to impose that the normal component of the electric field ($E_z$) be continuous at the interfaces $x = 0$ and $x = -L$ (assuming that the helices stand in air) [47, 48]. Such an ABC guarantees that the microscopic electric current that flows along each helical-shaped wire vanishes at both interfaces. Imposing the ABC and the classical boundary conditions, we obtain a $6 \times 6$ linear system which can be easily solved numerically with respect to the unknowns.

Using the outlined formalism it is possible to calculate analytically the transmission coefficient for plane wave incidence. The negative refraction at the interfaces between the slab of helical-shaped wires and air can be investigated using the approach proposed in [10], which is based on the variation in the phase of $t(\omega, \mathbf{k}) = |t|\, e^{j\phi}$ ($\phi = \arg t$) with $k_x$. It was proven in [10] that the spatial shift $\Delta$ suffered by an incoming beam when it crosses an arbitrary slab (see figure 8(a)) is equal to the slope of $\phi$, i.e. $\Delta = d\phi/dk_x$. In particular, negative refraction occurs when $\Delta$ is negative or, equivalently, when $\phi$ decreases with $k_x$. It is worth noting that such a method is completely general, and the only assumption is that the amplitude of the transmission coefficient varies slowly with $k_x$ within the band of spatial frequencies of the incoming beam [10].

In figures 8(b) and (c), we plot the amplitude and phase of the transmission coefficient as a function of the normalized transverse component of the wave vector $k_x$, obtained with the non-local homogenization model (solid lines), local homogenization model (dashed lines) and full-wave simulations (discrete symbols) [46]. It is important to highlight the good agreement between the results obtained from the three different calculation methods, especially for the example where the helix pitch $p$ is the shortest one and the frequency of operation is not excessively close to plasma frequency $\beta_{p,\text{eff}}a \approx 0.418$ [figures 8(b) and (c)(i)]. At frequencies close to $\beta_{p,\text{eff}}$ the local homogenization results become less accurate, as can be seen from
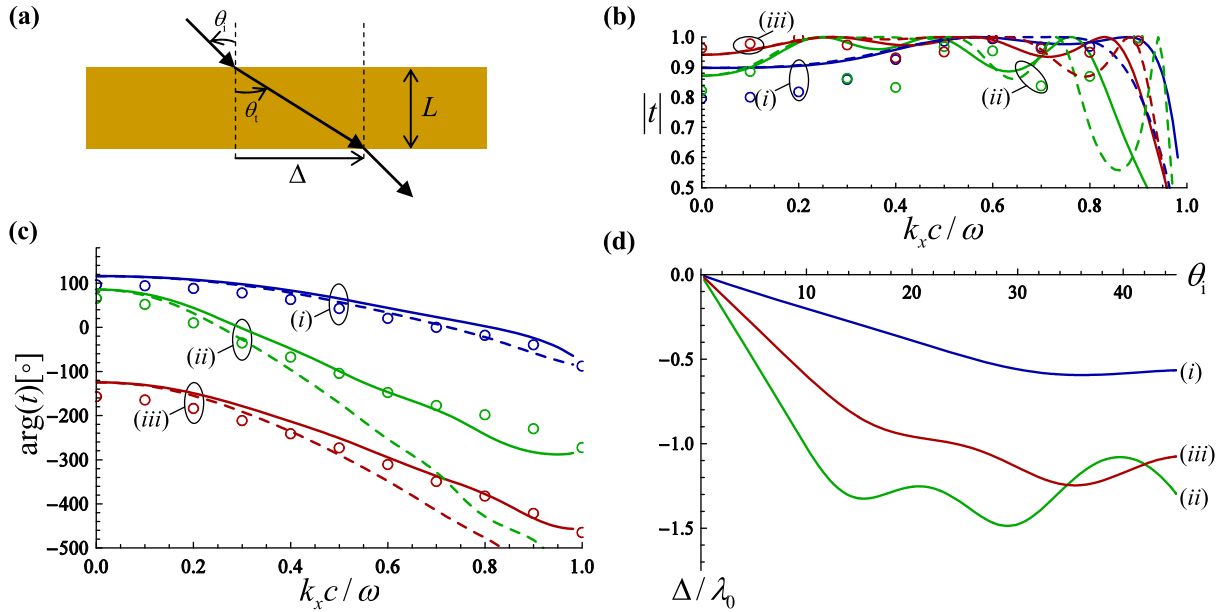
**(a)**

**(b)**

**(c)**

**(d)**

**Figure 8.** (a) Illustration of the spatial shift $\Delta$ suffered by a beam that illuminates an arbitrary slab. (b) Amplitude and (c) phase of the transmission coefficient as a function of the normalized $k_x$ for different metamaterial configurations. Solid lines: non-local homogenization results (equation (2)); dashed lines: local homogenization results (equation (10)); discrete symbols: full-wave results [46]. (d) Spatial shift $\Delta$ as a function of the angle of incidence $\theta_i$ for different configurations calculated using the analytical model based on the non-local homogenization theory. (i) $R = 0.4a$, $r_w = 0.05a$, $|p| = 0.3a$, $\omega a/c = 0.35$ and $L = 7a$; (ii) $R = 0.4a$, $r_w = 0.05a$, $|p| = 0.3a$, $\omega a/c = 0.4$ and $L = 7a$; (iii) $R = 0.4a$, $r_w = 0.05a$, $|p| = 0.5a$, $\omega a/c = 0.55$ and $L = 10a$.

figures 8(b) and (c)(ii). Similarly, the results predicted by the local homogenization model for configurations with longer helix pitch $p$ are also less accurate (figures 8(b) and (c)(iii)). This is entirely consistent with the fact that the spatial dispersion effects are only suppressed when $|p|/(2\pi R) \ll 1$, as already discussed in section 3.

On the other hand, figure 8(b) shows that the amplitude of the transmission coefficient varies slowly with $k_x$ and is close to unity for all propagating waves, satisfying in this manner the requirement of [10], besides indicating that the effective medium is well matched to free space, even for wide incident angles. In addition, one can see in figure 8(c) that the phase of the transmission coefficient $\phi$ decreases steadily with $k_x$, which undoubtedly proves the emergence of negative refraction at the interfaces of the considered metamaterial slab. This is further substantiated by figure 8(d), which depicts the spatial shift $\Delta$ as a function of $\theta_i$ obtained using our analytical model. It can be seen that $\Delta$ is indeed always negative for any positive angle of incidence $\theta_i$. In fact, the negative refraction effect in the metamaterial slab formed by helical-shaped wires may be quite strong, particularly for frequencies slightly below the plasma frequency $\beta_{p,\text{eff}}$ (equation (11)), as discussed previously. For instance, for $\omega a/c = 0.4$, an incoming beam with $\theta_i = 33°$ undergoes a spatial shift $\Delta = -1.35\lambda_0$ when it crosses a metamaterial slab with a thickness of only $L = 0.45\lambda_0$ (figure 8(d)(ii)). As
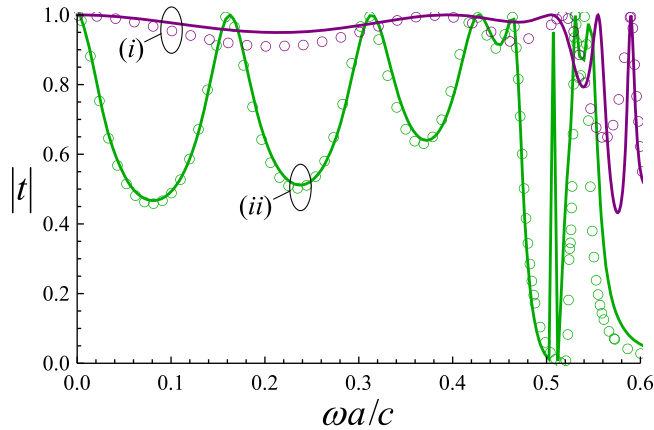
**Figure 9.** Amplitude of the transmission coefficient as a function of the normalized frequency for (i) a racemic helical wire medium and for (ii) a mushroom-type metamaterial [33], under plane-wave incidence with $\theta_i = 30°$. Solid lines: homogenization results (based on equation (2) for the helical wire medium, and based on equation (11) of [34] for the mushroom-type metamaterial); discrete symbols: full-wave results [46]. (i) $R = 0.4a$, $r_w = 0.05a$, $|p| = 0.4a$, $L = 4a$ and $\varepsilon_h = 1$; (ii) $g = 0.1a$, $r_w = 0.025a$, $h = a$, $L = 4a$ and $\varepsilon_h = 10.2$. The definition of the structural parameters of the multilayered mushroom is as in [33].

expected, the negative refraction effect becomes progressively weaker away from the frequency corresponding to $\varepsilon_{zz} = 0$. However, the negative refraction effect can be observed over a wide frequency band within the range wherein $\varepsilon_{zz} < 0$. For example, for $\omega a/c = 0.35$ an incoming beam with $\theta_i = 33°$ still suffers a considerable spatial shift $\Delta = -0.59\lambda_0$, even though the thickness of the slab is only $L = 0.39\lambda_0$ (see figure 8(d)(i)). It can be verified (not shown here) that the negative refraction is observed over nearly 60% of the frequency range below the plasma frequency $\omega/c = \beta_{p,\text{eff}}$. Of course, for frequencies corresponding to $\varepsilon_{zz} > 0$ an incoming beam is positively refracted.

As already mentioned in the introduction, the effects of spatial dispersion in the wire medium can also be suppressed by loading the wires with metallic patches (mushroom-type metamaterial [33]). It is thus interesting to compare the performance of the racemic helical wire medium with the multilayered mushroom structure. To this end, in figure 9 we show the amplitude of the transmission coefficient as a function of the frequency for both configurations and an incidence angle $\theta_i = 30°$. The two metamaterial slabs were designed to have the same physical thickness and similar plasma frequencies ($\beta_{p,\text{eff}}a \approx 0.5$).

As one can see from figure 9, the transmission coefficient of the racemic helical wire medium slab has amplitude very close to unity in the frequency range of interest ($\omega a/c < \beta_{p,\text{eff}}a$). In contrast, the level of transmission of the multilayered mushroom slab varies considerably with the frequency. These results are clear proof that the metamaterial considered in this work is much better matched to the air region, as compared to the multilayered mushroom structure. This is a consequence of the fact that the transverse permittivity of the mushroom-type medium may be quite large due to high-dielectric constant substrate and due to the presence of the metallic patches.
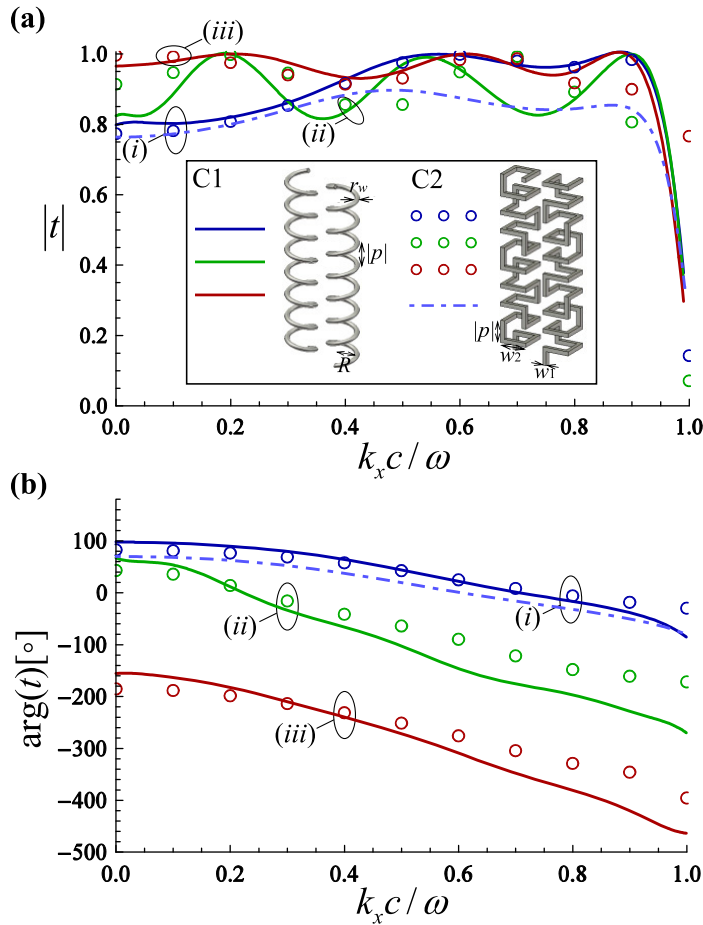
**Figure 10.** Full-wave calculation [46] of the amplitude (a) and phase (b) of the transmission coefficient as a function of the normalized $k_x$ for a racemic medium formed by cylindrical helices (solid lines) and for a modified structure formed by segmented helices (discrete symbols). (i) $R = 0.4a$, $r_w = 0.05a$, $|p| = 0.3a$, $\omega a/c = 0.35$ and $L = 7a$; (ii) $R = 0.4a$, $r_w = 0.05a$, $|p| = 0.3a$, $\omega a/c = 0.4$ and $L = 7a$; (iii) $R = 0.4a$, $r_w = 0.05a$, $|p| = 0.5a$, $\omega a/c = 0.55$ and $L = 10a$. The dot-dashed light blue curves in (i) are associated with a metamaterial formed by Ag segmented helices with $a = 2.5\,\mu$m, $r_w = 0.05a \approx 125$ nm, $R = 0.4a = 1.0\,\mu$m, $|p| = 0.3a \approx 0.75\,\mu$m and a frequency of operation $f = 6.68$ THz. Note that in the modified configuration (C2 in the inset of (a)) $R$ and $r_w$ are replaced by $w_1 = \sqrt{\pi}\, r_w$ and $w_2 = w_1 + (l_p - |p|)/3$, where $l_p = \sqrt{(2\pi R)^2 + |p|^2}$ represents the length of a cylindrical helix turn.

Next, we consider a variant of the racemic helical wire medium that is formed by 'segmented' helices (see the inset of figure 10). The motivation for this alternative structure is that it may be much easier to fabricate using printed circuit technology, based on a planar design with several layers of dielectric boards with printed metallic strips interconnected by vias, similar to mushroom structures [31, 32].

In order that this modified structure (C2 in the inset of figure 10) may mimic closely the electromagnetic response of the original structure (C1 in the inset of figure 10), the area of the transverse cross-section of the metallic wires as well as the volume fraction of metal in the unit cell are chosen to be the same as those in the configuration of cylindrical helices. As a result, we define the following equivalent geometrical parameters for the modified geometry: $w_1 = \sqrt{\pi} r_{\mathrm{w}}$ and $w_2 = w_1 + (l_p - |p|)/3$ (see the inset of figure 10), where $l_p = \sqrt{(2\pi R)^2 + |p|^2}$ represents the length of a cylindrical helix turn.

To verify the validity of the equivalent parameters for the segmented helices, the transmission coefficients for the two configurations (C1 and C2) are compared in figure 10, which reveals quite good agreement between the two cases. The results were obtained using the full-wave electromagnetic simulator [46]. Hence, it is expected that the modified configuration can mimic closely the electromagnetic response of the original configuration formed by cylindrical helices and enable a strong negative refraction effect.

In the previous discussions, it was assumed that the helical-shaped wires are PECs. To assess the effect of metallic loss, we have also calculated the transmission coefficient for a helical wire medium (dot-dashed lines in figure 10) formed by segmented Ag helices. It was assumed that Ag follows the Drude dispersion model, $\varepsilon_m = \varepsilon_\infty - \omega_p^2/(\omega(\omega - \mathrm{j}\Gamma))$, with parameters taken from the literature [49]. It is evident from figure 10 that even though there is a slight decrease of the transmission for wide incident angles, $|t|$ remains at quite a satisfactory level. On the other hand, the slope of the phase of the transmission coefficient remains very similar to the PEC result (see figure 10(b)(i)), confirming the emergence of a strong negative refraction, even when metal loss is taken into account. In fact, in general the effect of metallic losses is expected to be negligible provided that the skin depth $\delta_{\mathrm{s}}$ of the metal is smaller than the radius of the wires (in this example $r_{\mathrm{w}} = 5\delta_{\mathrm{s}}$) [10].

### 4.3. Gaussian beam excitation

To further confirm the findings of sections 4.1 and 4.2 and demonstrate in a conclusive manner the appearance of negative refraction, next we consider the scenario wherein the metamaterial slab is illuminated by an incoming Gaussian beam with transverse magnetic polarization (TM-$z$ polarized). Firstly, we use the non-local homogenization model to characterize the refraction of a Gaussian beam at the interfaces of a metamaterial slab infinitely extended along the $x$- and $y$-directions. In a later stage, in order to validate the homogenization results, the electromagnetic response of a finite-width metamaterial slab illuminated by a beam with Gaussian profile is simulated using CST Microwave Studio [46].

We consider a cylindrical Gaussian beam excitation with beam waist $w_0$, angle of incidence $\theta_{\mathrm{i}}$, focused at $z = z_0$ in front of the metamaterial slab (figure 5). The normalized magnetic field associated with the Gaussian beam excitation can be expanded into a Fourier integral of plane waves (spatial Fourier harmonics),

$$H_y^{\mathrm{GB}}(x, z) = \int_{-\infty}^{\infty} H_y^{\mathrm{GB}}(\omega, k_x)\, \mathrm{e}^{\gamma_0(z-z_0)}\, \mathrm{e}^{-\mathrm{j}k_x x}\, \mathrm{d}k_x, \quad \text{where } H_y^{\mathrm{GB}}(\omega, k_x) = \frac{\mathrm{e}^{-\frac{1}{4}\left(k_x - \frac{\omega}{c}\sin\theta_{\mathrm{i}}\right)w_0^2}\, w_0}{2\sqrt{\pi}}.$$

(14)

The response of the system to this excitation can be obtained by superposing the responses of the metamaterial to each individual plane wave of (14). Thus, the magnetic field in the three
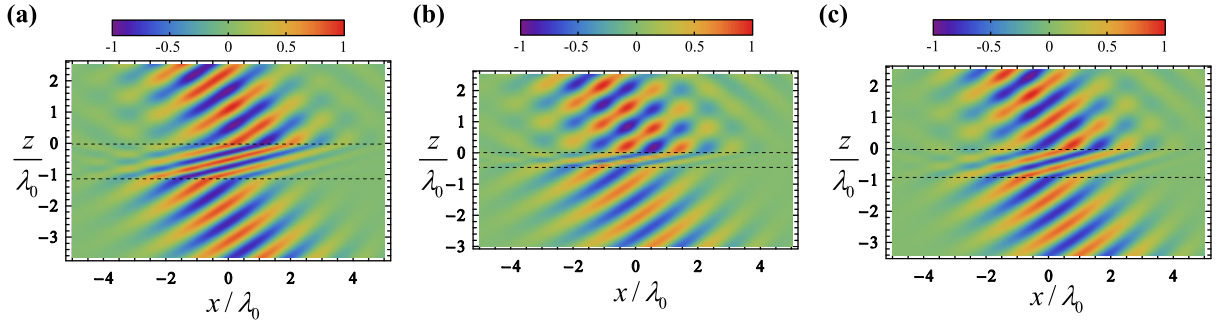
**Figure 11.** Time snapshot of the normalized magnetic field $H_y(t=0)$ calculated from equation (15). A Gaussian beam with TM polarization characterized by $2w_0 = 4\lambda_0$ and an incident angle of $\theta_i = 33°$ illuminates a structured slab formed by helical shaped wires. The metamaterial slab is periodic along the $x$- and $y$-directions. The black dashed lines represent the interfaces of the slab. (a) $R = 0.4a$, $r_w = 0.05a$, $|p| = 0.3a$, $\omega a/c = 0.35$ and $L = 20a$; (b) $R = 0.4a$, $r_w = 0.05a$, $|p| = 0.3a$, $\omega a/c = 0.4$ and $L = 7a$; (c) $R = 0.4a$, $r_w = 0.05a$, $|p| = 0.5a$, $\omega a/c = 0.55$ and $L = 10a$.

regions of space can be written as follows:

$$H_y^{(1)}(x,z) = \int_{-\infty}^{\infty} H_y^{GB}(\omega, k_x)(e^{\gamma_0(z-z_0)} + \rho(\omega, k_x)e^{-\gamma_0(z+z_0)})e^{-jk_x x}\,dk_x, \quad z > 0,$$

$$H_y^{(2)}(x,z) = \int_{-\infty}^{\infty} H_y^{GB}(\omega, k_x)H_y^{(2)}(k_x, z)e^{-\gamma_0 z_0}\,e^{-jk_x x}\,dk_x, \quad -L < z < 0,$$

$$H_y^{(3)}(x,z) = \int_{-\infty}^{\infty} H_y^{GB}(\omega, k_x)t(\omega, k_x)e^{\gamma_0(z+L-z_0)}\,e^{-jk_x x}\,dk_x, \quad z < -L, \tag{15}$$

where $H_y^{GB}(\omega, k_x)$ is given by equation (14), $H_y^{(2)}(k_x, z)$ is the magnetic field inside the slab ($-L < z < 0$) and defined in equation (12), and $\rho(\omega, k_x)$ and $t(\omega, k_x)$ are the reflection and transmission coefficients obtained by solving the plane wave scattering problem outlined in section 4.2. Using the above equations we can calculate the magnetic field profile in all regions of space.

In figure 11 we represent time snapshots ($t = 0$) of the magnetic field associated with a Gaussian beam characterized by an angle of incidence $\theta_i = 33°$ and a beam waist $2w_0 = 4\lambda_0$ for different structural parameters, calculated from equation (15). In all the figures it is manifest that the beam undergoes a significant negative spatial shift $\Delta$, demonstrating the emergence of strong negative refraction. The spatial shift suffered by the Gaussian beam, calculated by inspection of the maximum amplitude of the magnetic field profiles at the input and output interfaces, is (a) $\Delta \approx -1.65\lambda_0$, (b) $\Delta \approx -1.38\lambda_0$, and (c) $\Delta \approx -1.21\lambda_0$. These values are very much consistent with the results for the spatial shift $\Delta$ shown in figure 8(d), and calculated from the slope of the phase of the transmission coefficient. It is also evident from the results of figure 11 that the considered metamaterial slab is well matched to free space, since the wave reflection at both interfaces is almost imperceptible. This is completely consistent with the high magnitude of the transmission coefficient observable in figure 8(b).
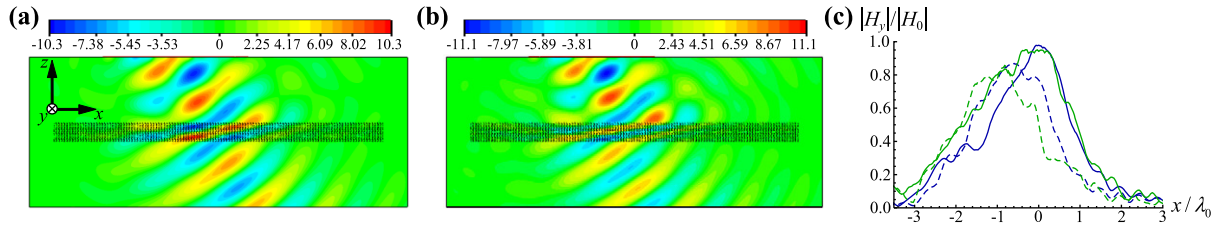
**Figure 12.** Time snapshot of the magnetic field $H_y(t = 0)$ (A m$^{-1}$) obtained from full-wave simulations done in the electromagnetic simulator [46]. A TM-polarized Gaussian beam characterized by $2w_0 = 3\lambda_0$ and with an incident angle $\theta_i = 33°$ illuminates a finite-width metamaterial slab formed by segmented helices (see the inset of figure 10). The metamaterial slab is finite along the $x$-direction, with width $W_x$, and is periodic along the $y$-direction with lattice period $a = 5$ mm. The remaining geometrical parameters of the structure are: $w_1 = 0.05\sqrt{\pi}a$, $w_2 \approx 0.832a$, $|p| = 0.3a$ and $L = 7a$; (a) $\omega a/c = 0.35$ ($f = 3.34$ GHz), (b) $\omega a/c = 0.4$ ($f = 3.82$ GHz). (c) Normalized magnetic field profile of the Gaussian beam at the input interface (solid lines) and at the output interface (dashed lines) for the cases (a) (blue lines) and (b) (green lines).

In order to confirm the previous results based on homogenization theory, we have simulated the electromagnetic response of the metamaterial slab under similar conditions using the commercial electromagnetic simulator [46]. However, due to the difficulty in modeling the structure formed by cylindrical helices (C1 in the inset of figure 10) in CST Microwave Studio, we have simulated instead the electromagnetic response of the modified configuration formed by segmented helices (C2 in the inset of figure 10). The structured slab is assumed to be periodic along the $y$-direction with period $a$ and finite along the $x$-direction with width $W_x = 122a$. In all the simulations, the lattice constant was taken as equal to $a = 5$ mm. The incoming cylindrical beam is uniform along the $y$-direction and has Gaussian beam profile along the $x$-direction, with a beam waist $2w_0 = 3\lambda_0$ at the frequency of operation. The angle of incidence is $\theta_i = 33°$. In all the simulations, the dielectric host is assumed to be air and the effects of metallic losses are taken into account by assuming that the metallic elements are made of copper ($\sigma = 5.8 \times 10^7$ S m$^{-1}$).

The time snapshots ($t = 0$) of the normal ($y$-component) of the magnetic field obtained with CST Microwave Studio for two different frequencies of operation are depicted in figures 12(a) and (b), and are qualitatively consistent with the homogenization results shown in figure 11 for the original metamaterial structure formed by cylindrical helices. The magnetic field profiles at the input (solid lines) and output (dashed lines) interfaces of the structured slab are depicted in figure 12(c). They undoubtedly show that the Gaussian beam is negatively refracted by the metamaterial slab. The values for the spatial shift inferred from figure 12(c) for the cases associated with panels (a) and (b) are, respectively, $\Delta \approx -0.6\lambda_0$ and $\Delta \approx -1.2\lambda_0$, which are reasonably consistent with the values of $\Delta$ obtained from the homogenization model of the configuration formed by cylindrical helices (see figure 8(d) and the discussion of the results of figure 11). Hence, these results further demonstrate that the modified metamaterial configuration formed by segmented helices mimics the electromagnetic response of the homogenized structure formed by cylindrical helices. It is also worth noting that, similar to the original structure (figure 11), in the modified configuration formed by segmented helices the level of reflection is also very weak, and hence the metamaterial is well matched to free space.

## 5. Partial focusing by a planar lens

In the following, we investigate the possibility of taking advantage of the negative refraction effect to obtain partial focusing of the electromagnetic waves by a planar metamaterial lens [19, 20].

### 5.1. Guidelines for the design of the flat lens

To begin with, we briefly discuss how to fix the thickness $L$ of the metamaterial so that the electromagnetic radiation of a point source placed at a distance $d_1$ from the front interface is partially focused at a distance $d_1 = d_2$ from the back interface (see the inset of figure 13(a)). As proven in [11], the required normalized thickness $L$ for the lens is given by the following formula:

$$\frac{L}{d_1} = 2 \left| \frac{\tan \theta_i}{\tan \theta_t} \right|. \tag{16}$$

Based on this equation, we computed the required normalized thickness $L$ for the lens as a function of the angle of incidence $\theta_i$ for two different slab configurations (figure 13(a)). We show only the curve associated with each configuration for positive or negative angles of incidence, since it is evident that, by symmetry, $L(\theta_i)$ is an even function of $\theta_i$.

As seen from figure 13(a), the required thickness $L$ for the slab is not constant, but instead it is angle dependent. In fact, this result could be expected and is simply a consequence of the nonlinear relation between the angle of incidence $\theta_i$ and the angle of transmission $\theta_t$ (see figure 7). This angle dependence implies that, unlike in Veselago's lens, the light rays will not converge into a single point. Nevertheless, the metamaterial lens enables a partial focusing of the electromagnetic radiation [19, 20]. In order to illustrate this possibility, we represent in figure 13(b) the ray-tracing diagrams showing the path of the rays inside and outside the slab for $d_1 = 0.5L$, which is a value consistent with the plots of figure 13(a). Clearly, the rays coming from the line source (located above the slab) are partially refocused inside the metamaterial lens, and also after crossing the lens at a partial focus located at a distance $d_1 \approx d_2$ from the back interface.

### 5.2. Imaging a magnetic line source

To verify the ray-tracing diagrams and to further characterize the imaging properties of the considered structured lens, in the following we consider that a magnetic line source (infinitely extended along the $y$-direction) is placed at a distance $d_1$ above the metamaterial slab (figure 14(a)). The magnetic field radiated by the line source is of the form $H_y = (A/4j)H_0^{(2)}((\omega/c)\rho)$, where $A$ is a constant that depends on the line current, $\rho$ is the radial distance to the source, and $H_0^{(2)}(x) = J_0(x) - jY_0(x)$ is the Hankel function of the second kind and order zero. The field of a line source can be decomposed into a spectrum of plane waves, i.e. the Hankel function can be represented as a Fourier integral of plane waves. Hence, considering that the magnetic line source is located at $z = d_1$, its magnetic field is of the form:

$$H_y(x, z) = \frac{A}{\pi} \int_0^\infty \frac{1}{2\gamma_0} e^{-\gamma_0 |z - d_1|} \cos(k_x x) \, dk_x. \tag{17}$$
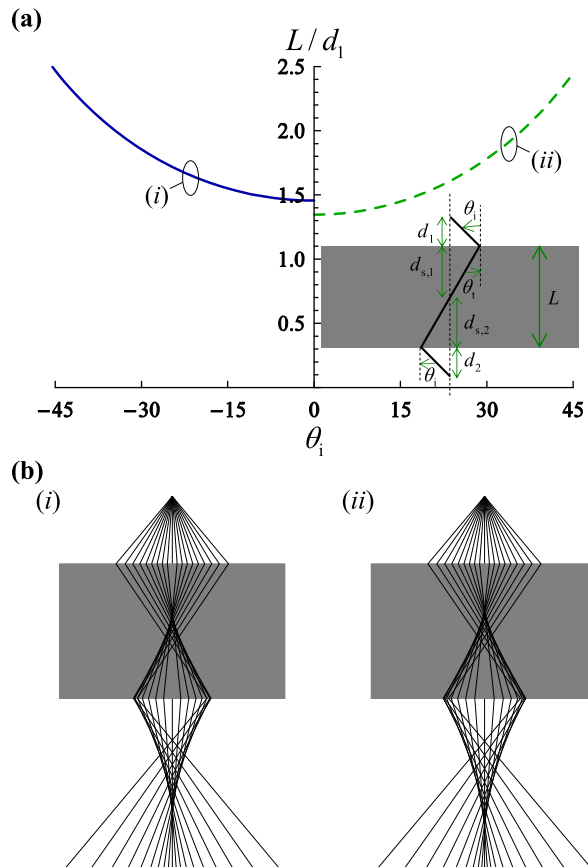
**(a)**



**(b)**



**Figure 13.** (a) Normalized thickness of the metamaterial slab as a function of the angle of incidence calculated such that $d_1 = d_2$. (i) $R = 0.4a$, $r_w = 0.05a$, $|p| = 0.3a$ and $\omega a/c = 0.28$; (ii) $R = 0.4a$, $r_w = 0.05a$, $|p| = 0.5a$ and $\omega a/c = 0.45$. The inset represents the geometry of the problem. (b) Ray-tracing diagrams showing that the structured material refocuses the rays coming from a magnetic line source both inside and outside the slab. The rays represent the direction of the Poynting vector (energy density flux). The source is placed at a distance $d_1 = 0.5L$ from the front interface, the thickness of the slab is $L = 20a$, and the remaining parameters are the same as in (a): (i) the same parameters as (a$i$) and (ii) the same parameters as (a$ii$).

Now, similarly to what was done in the derivation of equation (15), the magnetic field in the three space regions can be written in terms of Sommerfeld-type integrals:

$$H_y^{(1)}(x, z) = \frac{A}{\pi} \int_0^\infty \frac{1}{2\gamma_0} (e^{-\gamma_0 |z-d_1|} + \rho(\omega, k_x) e^{-\gamma_0(z+d_1)}) \cos(k_x x) \, dk_x, \quad z > 0,$$

$$H_y^{(2)}(x, z) = \frac{A}{\pi} \int_0^\infty \frac{1}{2\gamma_0} H_y^{(2)}(k_x, z) e^{-\gamma_0 d_1} \cos(k_x x) \, dk_x, \quad -L < z < 0,$$

$$H_y^{(3)}(x, z) = \frac{A}{\pi} \int_0^\infty \frac{1}{2\gamma_0} t(\omega, k_x) e^{\gamma_0(z+L-d_1)} \cos(k_x x) \, dk_x, \quad z < -L, \qquad (18)$$
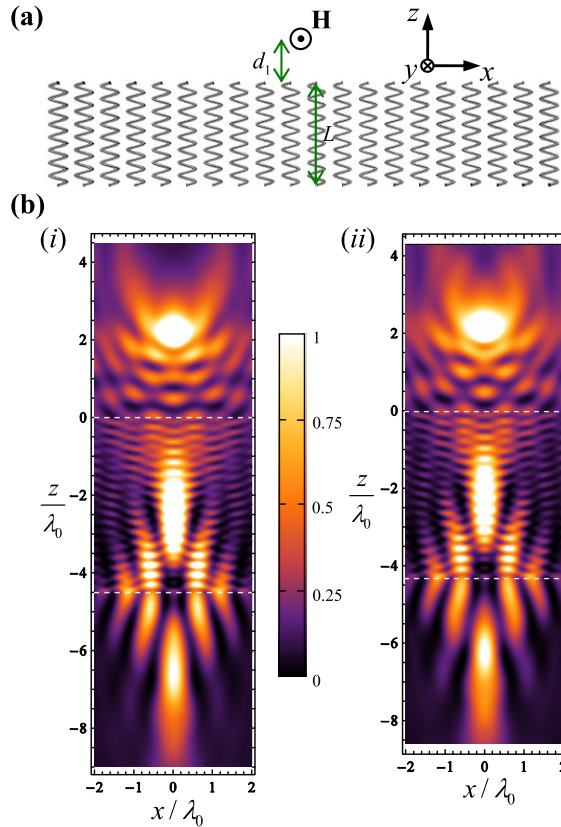
**Figure 14.** (a) Geometry of the problem: a magnetic line source is placed at a distance $d_1$ above the helical wire medium lens. (b) Squared (normalized) amplitude of the magnetic field $|\mathbf{H}|^2$. (i) $R = 0.4a$, $r_\mathrm{w} = 0.05a$, $|p| = 0.3a$, $\omega a/c = 0.28$ and $L = 100a$; (ii) $R = 0.4a$, $r_\mathrm{w} = 0.05a$, $|p| = 0.5a$, $\omega a/c = 0.45$ and $L = 60a$. The white dashed lines represent the interfaces of the slab.

where $H_y^{(2)}(k_x, z)$ is the magnetic field inside the slab $(-L < z < 0)$ and is defined as in equation (12), and $\rho(\omega, k_x)$ and $t(\omega, k_x)$ are the reflection and transmission coefficients obtained by solving the plane wave scattering problem outlined in section 4.2. Using this formalism, we calculated the magnetic field profile in all regions of space.

In figure 14(b) the density plots of the normalized squared amplitude of the magnetic field $|\mathbf{H}|^2$ are depicted in the *xoz*-plane for the same metamaterial configurations of the ray-tracing diagrams of figure 13(b).

In both figures, an intense and elongated focal point of the magnetic field inside the helical wire medium lens and also after the lens is clearly seen. The slight aberration along the *z*-direction is consistent with the ray-tracing diagrams of figure 13(b). These results prove that a thick enough slab of the metamaterial can work, indeed, as a planar focusing device, redirecting the electromagnetic radiation of a *p*-polarized source to a narrow spot at the focal plane. Moreover, consistent with the results of section 4.3 for a Gaussian beam excitation (see figure 11), it is visible from figure 14(b) that the non-bianisotropic helical wire medium lens is well matched to free space, since field reflections are hardly noticeable in the region above the lens (where the source is located).

The resolution of this structured lens is limited by diffraction, since the half-power beamwidth (HPBW) at the focal plane is about $\lambda_0/2$ as in any conventional optical system. Nevertheless, and despite the referred resolution restriction, the considered metamaterial lens has the important property that the imaging characteristics are independent of the position of the source because of the flat interfaces.

## 6. Conclusion

We have shown that a metamaterial formed by a racemic mixture of helical-shaped wires may effectively behave as a local (with a very much reduced spatial dispersion) uniaxial ENG material and, as a result, enable a strong negative refraction effect over a wide frequency band. The proposed metamaterial is an interesting alternative to the arrays of metallic wires loaded with metallic patches (multilayered mushroom-type metamaterial), and may have the advantage of being better matched to the surrounding medium (e.g. free space), and hence enabling a lower level of reflections. Taking advantage of the negative refraction effect, we have demonstrated the possibility of using the proposed metamaterial to design a planar lens that provides partial focusing. The reported results were obtained using an effective medium model and confirmed by full-wave simulations [46].

## References

[1] Veselago V G 1968 *Sov. Phys. Usp.* **10** 509
[2] Pendry J B 2000 *Phys. Rev. Lett.* **85** 3966
[3] Smith D R, Padilla W J, Vier D C, Nemat-Nasser S C and Schultz S 2000 *Phys. Rev. Lett.* **84** 4184
[4] Shelby R A, Smith D R and Schultz S 2001 *Science* **292** 77
[5] Valentine J, Zhang S, Zentgraf T, Ulin-Avila E, Genov D A, Bartal G and Zhang X 2008 *Nature* **455** 376
[6] Garcia N and Nieto-Vesperinas M 2002 *Phys. Rev. Lett.* **88** 207403
[7] Smith D R, Schurig D, Rosenbluth M, Schultz S, Ramakrishna S A and Pendry J B 2003 *Appl. Phys. Lett.* **82** 1506
[8] Notomi M 2000 *Phys. Rev.* B **62** 10696
[9] Cubukcu E, Aydin K, Ozbay E, Foteinopoulou S and Soukoulis C M 2003 *Nature* **423** 604
[10] Silveirinha M G 2009 *Phys. Rev.* B **79** 153109
[11] Morgado T A and Silveirinha M G 2010 *Metamaterials* **4** 112–118
[12] Tretyakov S, Nefedov I, Sihvola A, Maslovski S and Simovski C 2003 *J. Electromagn. Waves Appl.* **17** 695
[13] Pendry J 2004 *Science* **306** 1353–1355
[14] Zhang S, Park Y-S, Li J, Lu X, Zhang W and Zhang X 2009 *Phys. Rev. Lett.* **102** 023901
[15] Maslovski S I and Tretyakov S A 2003 *J. Appl. Phys.* **94** 4241–4243
[16] Pendry J B 2008 *Science* **322** 71–73
[17] Maslovski S I and Tretyakov S A 2012 *New J. Phys.* **14** 035007
[18] Lindell I V, Tretyakov S A, Nikoskinen K I and Ilvonen S 2001 *Microw. Opt. Technol. Lett.* **31** 129
[19] Smith D R and Schurig D 2003 *Phys. Rev. Lett.* **90** 077405
[20] Smith D R, Schurig D, Mock J J, Kolinko P and Rye P 2004 *Appl. Phys. Lett.* **84** 2244
[21] Fan X, Wang G P, Lee J C W and Chan C T 2006 *Phys. Rev. Lett.* **97** 073901
[22] Hoffman A J, Alekseyev L, Howard S S, Franz K J, Wasserman D, Podolskiy V A, Narimanov E E, Sivco D L and Gmachl G 2007 *Nature Mater.* **6** 946
[23] Fang A, Koschny T and Soukoulis C M 2009 *Phys. Rev.* B **79** 245127
[24] Liu Y, Bartal G and Zhang X 2008 *Opt. Express* **16** 15439

[25] Yao J, Liu Z, Liu Y, Wang Y, Sun C, Bartal G, Stacy A M and Zhang X 2008 *Science* **321** 930

[26] Belov P A, Marqués R, Maslovski S I, Nefedov I S, Silveirinha M, Simovski C R and Tretyakov S 2003 *Phys. Rev.* B **67** 113103

[27] Demetriadou J and Pendry J B 2008 *J. Phys.: Condens. Matter* **20** 295222

[28] Maslovski S I and Silveirinha M G 2009 *Phys. Rev.* B **80** 245101

[29] Luukkonen O, Silveirinha M G, Yakovlev A B, Simovski C R, Nefedov I S and Tretyakov S A 2009 *IEEE Trans. Microw. Theory Tech.* **57** 2692

[30] Luukkonen O, Silveirinha M G, Yakovlev A B, Simovski C R, Nefedov I S and Tretyakov S A 2009 *IEEE Trans. Microw. Theory Tech.* **57** 2700

[31] Luukkonen O, Alitalo P, Costa F, Simovski C, Monorchio A and Tretyakov S 2010 *Appl. Phys. Lett.* **96** 081501

[32] Lockyear M J, Hibbins A P and Sambles J R 2009 *Phys. Rev. Lett.* **102** 073901

[33] Silveirinha M G and Yakovlev A B 2010 *Phys. Rev.* B **81** 233105

[34] Kaipa C S R, Yakovlev A B and Silveirinha M G 2011 *J. Appl. Phys.* **109** 044901

[35] Yatsenko V V, Tretyakov S A and Sochava A A 1998 *Int. J. Appl. Electromagn. Mech.* **9** 191–200

[36] Belov P A, Simovski C R and Tretyakov S A 2003 *Phys. Rev.* E **67** 056622

[37] Gansel J K, Tiel M, Rill M S, Decker M, Bade K, Saile V, von Freymann G, Linden S and Wegener M 2009 *Science* **325** 1513–1515

[38] Gansel J K, Wegener M, Burger S and Linden S 2010 *Opt. Express* **18** 1059

[39] Wu C, Li H, Yu X, Li F, Chen H and Chan C T 2011 *Phys. Rev. Lett.* **107** 177401

[40] Silveirinha M G 2008 *IEEE Trans. Antennas Propag.* **56** 390 also available online at http://arxiv.org/abs/cond-mat/0701118

[41] Silveirinha M G 2007 *Phys. Rev.* B **75** 115104

[42] Agranovich V and Ginzburg V 1966 *Spatial Dispersion in Crystal Optics and the Theory of Excitons* (New York: Wiley-Interscience)

[43] Tretyakov S 2003 *Analytical Modeling in Applied Electromagnetics* (Norwood, MA: Artech House)

[44] Silveirinha M G 2009 *New J. Phys.* **11** 113016

[45] Silveirinha M G and Fernandes C A 2004 *IEEE Trans. Microw. Theory Tech.* **52** 889

[46] CST Microwave Studio 2010 http://www.cst.com

[47] Silveirinha M G 2006 *IEEE Trans. Antennas Propag.* **54** 1766

[48] Silveirinha M G, Fernandes C A and Costa J R 2008 *New J. Phys.* **10** 053011

[49] Ordal M A, Bell R J, Alexander R W, Long L L Jr and Querry M R 1985 *Appl. Opt.* **24** 4493